Journal of The Electrochemical Society

The Impact of Peltier and Dufour Coefficients on Heat Fluxes and Temperature Profiles in the Polymer Electrolyte Fuel Cells

Journal of The Electrochemical Society, 2020 **167** 144503

The Impact of Peltier and Dufour Coefficients on Heat Fluxes and Temperature Profiles in the Polymer Electrolyte Fuel Cells

Marco Sauermoser,[1,z] Signe Kjelstrup,[1,z] and Bruno G. Pollet[2]

[1]*PoreLab, Department of Chemistry, Norwegian University of Science and Technology, NTNU, Trondheim, Norway*
[2]*Department of Energy and Process Engineering, Norwegian University of Science and Technology, NTNU, Trondheim, Norway*

We show that the coupling effects in non-equilibrium thermodynamics for heat-, mass- and charge- transport in the polymer electrolyte membrane fuel cell (PEMFC) all give significant contributions to local heat effects. The set of equations was solved by modifying an open-source 1D fuel cell algorithm. The entropy balance was used to check for model consistency. The balance was obeyed within 10% error in all PEMFC layers, except for the cathode backing. The Dufour effect/thermal diffusion and the Peltier/Seebeck coefficient are commonly neglected. Here they are included systematically. The model was used to compute heat fluxes out of the cell. A temperature difference of 5 K between the left and right boundary of the system could change the heat fluxes up to 44%. The Dufour effect, for instance, increases the temperature of both anode and cathode, up to 9 K. The possibility to accurately predict local heat effects can be important for the design of fuel cell stacks, where intermediate cooling is central. This work is based on Paper 1484 presented at the Atlanta, Georgia, Meeting of the Society, October 13–17, 2019.

 [DOI: 10.1149/1945-7111/abc110]

Manuscript submitted August 14, 2020; revised manuscript received October 7, 2020. Published November 2, 2020.

List of symbols

σ	Entropy production [W K^{-1} m^3]
$\sigma^{a,lb}$	Entropy production in the anode PTL on the left system boundary side [W K^{-1} m^3]
$\sigma^{a,m}$	Entropy production in the anode PTL on the membrane side [K]
$\sigma^{c,m}$	Entropy production in the cathode PTL on the membrane side [K]
$\sigma^{m,a}$	Entropy production in the membrane on the anode PTL side [K]
$\sigma^{m,c}$	Entropy production in the membrane on the cathode PTL side [K]
σ^{s}	Entropy production of a surface [W K^{-1} m^2]
x	Through-plane coordinate [m]
dS_{irr}/dt	Total entropy production [W K^{-1}]
V	Volume [m^3]
Ω	Cross-sectional area [m^2]
J_s^{in}	Entropy flux into the (sub-)system [W K^{-1} m^2]
J_s^{out}	Entropy flux out of the (sub-)system [W K^{-1} m^2]
$J_s^{s,in}$	Entropy flux into the surface [W K^{-1} m^2]
$J_s^{s,out}$	Entropy flux out of the surface [W K^{-1} m^2]
J_{H_2}	Hydrogen flux [mol m^{-2} s]
J_{O_2}	Oxygen flux [mol m^{-2} s]
J_w	Water flux [mol m^{-2} s]
J_w^a	Water flux in the anode PTL [mol m^{-2} s]
J_w^m	Water flux in the membrane [mol m^{-2} s]
J_w^c	Water flux in the cathode PTL [mol m^{-2} s]
$J_w^{a,m}$	Water flux in the anode PTL on the membrane side [mol m^{-2} s]
$J_w^{c,m}$	Water flux in the cathode PTL on the membrane side [mol m^{-2} s]
$J_w^{m,a}$	Water flux in the membrane on the anode PTL side [mol m^{-2} s]
$J_w^{m,c}$	Water flux in the membrane on the cathode PTL side [mol m^{-2} s]
J_D	Interdiffusion flux [mol m^{-2} s]
j	Current density [A m^{-2}]
F	Farraday's constant [C mol^{-1}]
R	Gas constant [J K^{-1} mol]
J_u	Energy flux [J m^{-2} s]
J_q'	Measurable heat flux [J m^{-2} s]
$J_q'^a$	Measurable heat flux in the anode PTL [J m^{-2} s]
$J_q'^m$	Measurable heat flux in the membrane [J m^{-2} s]
$J_q'^c$	Measurable heat flux in the cathode PTL [J m^{-2} s]
$J_q'^{a,m}$	Measurable heat flux in the anode PTL on the membrane side [J m^{-2} s]
$J_q'^{c,m}$	Measurable heat flux in the cathode PTL on the membrane side [J m^{-2} s]
$J_q'^{m,a}$	Measurable heat flux in the membrane on the anode PTL side [J m^{-2} s]
$J_q'^{m,c}$	Measurable heat flux in the membrane on the cathode PTL side [J m^{-2} s]
H_{H_2}	Molar enthalpy of hydrogen [J mol^{-1}]
H_{O_2}	Molar enthalpy of oxygen [J mol^{-1}]
H_w^a	Molar enthalpy of water in the anode PTL [J mol^{-1}]
H_w^m	Molar enthalpy of water in the membrane [J mol^{-1}]
H_w^c	Molar enthalpy of water in the cathode PTL [J mol^{-1}]
$H_w^{m,a}$	Molar enthalpy of water in the membrane on the anode PTL side [J mol^{-1}]
$H_w^{c,m}$	Molar enthalpy of water in the cathode PTL on the membrane side [J mol^{-1}]
$H_w^{a,m}$	Molar enthalpy of water in the anode PTL on the membrane side [J mol^{-1}]
$H_w^{m,c}$	Molar enthalpy of water in the membrane on the cathode PTL side [J mol^{-1}]
$S_w^{0,m}$	Standard entropy of liquid water [J K^{-1} mol]
$S_w^{0,c}$	Standard entropy of vapor water [J K^{-1} mol]
$S_w^{a,m}$	Molar entropy of water in the anode PTL on the membrane side [J K^{-1} mol]
$S_w^{m,c}$	Molar entropy of water in the membrane on the cathode PTL side [J K^{-1} mol]
$c_{p,w}^m$	Specific heat capacity of liquid water [J K^{-1} mol]
$c_{p,w}^c$	Specific heat capacity of vapor water [J K^{-1} mol]
ϕ	Electric potential [V]
ϕ^a	Electric potential in the anode PTL [V]
ϕ^m	Electric potential in the membrane PTL [V]
ϕ^c	Electric potential in the cathode PTL [V]
$\phi^{m,a}$	Electric potential on the right side of the anode [V]
$\phi^{a,m}$	Electric potential on the left side of the anode [V]
$\phi^{c,m}$	Electric potential on the right side of the cathode [V]
$\phi^{m,c}$	Electric potential on the left side of the cathode [V]

[z]E-mail: marco.sauermoser@ntnu.no; signe.kjelstrup@ntnu.no

ϕ^{cell} Electric potential of the PEMFC [V]
$\Delta_{\text{a,m}}\phi_{eff}$ Effective electric potential at the anode [V]
$\phi^{\text{a,lb}}$ Electric potential in the anode PTL on the left system boundary side [V]
x_w Molar fraction of water [−]
x_w^{lb} Molar fraction of water at the left system boundary [−]
x_w^{rb} Molar fraction of water at the right system boundary [−]
$x_w^{\text{a,lb}}$ Molar fraction of water in the anode PTL on the left system boundary side [−]
$x_w^{\text{c,rb}}$ Molar fraction of water in the cathode PTL on the right system boundary side [−]
$x_w^{\text{c,m}}$ Molar fraction of water in the cathode PTL on membrane side [−]
x_i Molar fraction of component i [−]
x_w^* Molar fraction of water at saturation [−]
x_w^{entrance} Molar fraction of water in the cathode PTL on the membrane side [−]
a_w Water activity in the membrane [−]
a_w^{entrance} Water activity in the membrane on the anode PTL side [−]
$a_w^{\text{m,a}}$ Water activity in the membrane on the anode PTL side [−]
λ_w Water content in the membrane [mol water/mol membrane ionic site]
c Total concentration [mol m^{-3}]
T Temperature [K]
T' Temperature [°C]
T^{s} Temperature at the surface [K]
$T^{\text{a,m}}$ Temperature in the anode PTL on the membrane side [K]
$T^{\text{c,m}}$ Temperature in the cathode PTL on the membrane side [K]
$T^{\text{m,a}}$ Temperature in the membrane on the anode PTL side [K]
$T^{\text{m,c}}$ Temperature in the membrane on the cathode PTL side [K]
T^{lb} Temperature at the left system boundary [K]
T^{rb} Temperature at the right system boundary [K]
$T^{\text{a,lb}}$ Temperature in the anode PTL on the left system boundary side [K]
$T^{\text{c,rb}}$ Temperature in the cathode PTL on the right system boundary side [K]
$\mu_{w,T}$ Chemical potential of water at constant temperature [J mol^{-1}]
$\mu_{w,T}^0$ Chemical potential of water at constant temperature and standard conditions [J mol^{-1}]
$\mu_{w,T}^{\text{m,a}}$ Chemical potential of water at constant temperature in the membrane on the anode PTL side [J mol^{-1}]
$\mu_{w,T}^{\text{c,m}}$ Chemical potential of water at constant temperature in the cathode PTL on the membrane side [J mol^{-1}]
$\mu_{w,T}^{\text{a,m}}$ Chemical potential of water at constant temperature in the anode PTL on the membrane side [J mol^{-1}]
$\mu_{w,T}^{\text{m,c}}$ Chemical potential of water at constant temperature in the membrane on the cathode PTL side [J mol^{-1}]
$\Delta_n G^{\text{s}}$ Reaction Gibbs energy of neutral surface components [J mol^{-1}]
λ^{a} Thermal conductivity of the anode PTL [W m^{-1} K]
λ^{m} Thermal conductivity of the membrane [W m^{-1} K]
λ^{c} Thermal conductivity of the cathode PTL [W m^{-1} K]
$\lambda^{\text{s,a}}$ Thermal conductivity of the anode on the anode PTL side [W m^{-2} K]
$\lambda^{\text{s,m}}$ Thermal conductivity of the anode on the membrane side [W m^{-2} K]
$\lambda^{\text{s,c}}$ Thermal conductivity of the cathode on the cathode PTL side [W m^{-2} K]
π^{a} Peltier coefficient in the anode PTL [J]
π^{m} Peltier coefficient in the membrane [J]
π^{c} Peltier coefficient in the cathode PTL [J]
t_w^{a} Transference coefficient of water in the anode PTL [−]
t_w^{m} Transference coefficient of water in the membrane [−]
t_w^{c} Transference coefficient of water in the cathode PTL [−]
$D_{w\text{H}_2}^{\text{a}}$ Diffusivity coefficient of water in hydrogen in the anode PTL [m^2 s^{-1}]
D_w^{m} Diffusivity coefficient of water in the membrane [m^2 s^{-1}]
$D_{w\text{O}_2}^{\text{c}}$ Diffusivity coefficient of water in oxygen in the cathode PTL [m^2 s^{-1}]
r^{a} Electric resistance of the anode PTL [Ohm m]
r^{m} Electric resistance of the membrane [Ohm m]
r^{c} Electric resistance of the cathode PTL [Ohm m]
$r^{\text{s,a}}$ Electric resistance of the anode on the anode PTL side [Ohm m^2]
$r^{\text{s,c}}$ Electric resistance of the cathode on the cathode PTL side [Ohm m^2]
$q^{*,\text{a}}$ Heat of transfer in the anode PTL [J mol^{-1}]
$q^{*,\text{m}}$ Heat of transfer in the membrane [J mol^{-1}]
$q^{*,\text{c}}$ Heat of transfer in the cathode PTL [J mol^{-1}]
j_0 Exchange current density [A m^{-2}]
j_{0,H_2} Revised exchange current density at the anode [A m^{-2}]
j_{0,O_2} Revised exchange current density at the cathode [A m^{-2}]
j'_{0,H_2} Intrinsic exchange current density at the anode [A m^{-2}]
j'_{0,O_2} Intrinsic exchange current density at the cathode [A m^{-2}]
p^0 Standard pressure [atm]
p_{H_2} Partial pressure of hydrogen [atm]
p_{O_2} Partial pressure of oxygen [atm]
α Charge transfer coefficient of the electrode [−]
n Number of electrons involved in the cell reaction [−]
η Overpotential [V]
EPSA^{a} Electrochemical Pt surface area of the anode [cm^2 cm^{-2}]
EPSA^{c} Electrochemical Pt surface area of the cathode [cm^2 cm^{-2}]
l^{a} Anode PTL length [m]
l^{m} Membrane length [m]
l^{c} Cathode PTL length [m]

Electrochemical systems like fuel cells and batteries are becoming increasingly more important to realize a transition to renewable energy systems.[1,2] Activities to increase system efficiencies are high, and also central for economic competitiveness. A critical issue, say, for fuel cell stacks and lithium batteries alike, is the local heat production inside the cell. This plays an essential role for safety issues,[3] durability[4] and auxiliary equipment design (e.g. cooling equipment[5]) and therefore also system efficiency. Sufficiently detailed physical models are required to predict the cell behavior. This paper addresses the issue of local heat production, sources and sinks, in polymer electrolyte membrane fuel cells (PEMFC) in a more complete way than before. A preliminary version of the work was already presented.[6] For a similar analysis of the lithium battery, we refer to.[7]

The now dominant ways to model coarse-grained PEMFCs were developed during the last century.[8–10] In particular, there was an effort to define variables for a porous electrode. All physical models must obey the balance equations for mass, momentum and energy. In addition, there are constitutive equations of transport. These have often been a matter of choice, however. In order to be thermodynamically consistent, any choice must conform, not only with the conservation laws but also with the entropy balance. This applies to a control volume, and to the system as a whole. The only theory that addresses the entropy balance directly is non-equilibrium thermodynamics.[11] The extension of this general theory to heterogeneous systems was made in the 1970s, see Ref. 11 and references therein. It is capable of dealing with porous electrodes.[9,12,13] The cell is then divided into separate layers, each layer treated as an autonomous subsystem, with an entropy production, σ, assigned to it. Siemer et al.[14] and Huerta et al.[15] applied non-equilibrium thermodynamics to solid oxide fuel cells as well as PEMFCs.

The theory teaches us about the interaction (coupling) of the various phenomena in a cell layer, such as the electro-osmotic effect, the Soret/Dufour, and Seebeck/Peltier effects in addition to Fourier's,- Fick's,- and Ohm's law. When we want, e.g., to examine the thermal signature of the PEMFC, it is then not enough to only

compute the reversible heat effect from the overall entropy change of the cell.[16] Also, the Peltier, Dufour, or their reciprocal Seebeck and Soret-coefficients are needed to compute the local heat effects. These terms have not, or only partially, been taken into account in earlier models.[17,18] They are needed when the local variation in temperature, composition and dissipation matters.

The purpose of this work is thus to document in particular how the heat effects in the PEMFC can be modelled and understood using non-equilibrium thermodynamics, extending earlier work.[6,11,12,19] The method will be used to document:

(i) A set of simultaneous solutions for profiles of essential variables such as the electric potential, water concentration, and temperature, in addition to water- and heat flux-values across the cell
(ii) The effect of coupling terms, in particular, the commonly neglected Soret/Dufour and Seebeck/Peltier effects
(iii) The impact of these effects on the heat and water fluxes in and out of the cell
(iv) If the model obeys the entropy balance locally as well as globally
(v) Properties important to cell design

We will recapitulate the constitutive equations that can be used to solve the profiles mentioned.[11] The system, with its subsystems and excess variables, is first described. The theory for homogeneous layers and porous electrodes is recapitulated afterwards. The case studies include a Base Case computed using typical data from the literature. The model is implemented in an open-source 1D fuel cell code.[20] The modifications introduced by us are described in the solution procedure. A result presentation and discussion follows.

We shall conclude like Bvumbe et al.,[16] that it is crucial to model individual and local contributions to flux equations to gain a deeper, more fundamental understanding of the processes in the fuel cell and how they interact.

System

The PEMFC is sketched in Fig. 1. The membrane electrode assembly (MEA) is sandwiched between two porous transport layers (PTL), all held together by flow field plates (FFP). The current collector plate and the FFP are labelled 1 and 2, respectively. The porous transport layers are denoted by 3, the membrane by 5, while the electrocatalytic layers on the anode and cathode are labelled 4 and 6, respectively. Several issues are known to be critical for good cell performance cf.[21] The fuel gases need to be humidified to avoid membrane dry-out because each proton transported carry along 1–2 water molecules (electro-osmotic drag coefficient) across the membrane. We assume that water exits via the same or a separate flow field and consider one-dimensional transport perpendicular to the layers pictured in Fig. 1. There are adiabatic boundaries in the other dimensions. The positive direction of the fluxes is from left to right.

Layer definitions.—The reacting gases can enter on both sides via the flow field, and have access to the nanoporous catalyst via nano- and micro-porous layers as described in Fig. 1. In spite of knowledge of the finer micro-structure indicated in this figure, we describe three of the fuel cell layers as continuous, homogeneous phases, while the electrode layers will be treated discretely.

The continuous regions, with a row of control volumes (CV) after each other, are indicated in Fig. 2 (left) by CV1, CV2 and CV3. In Fig. 2 (left), they are represented by layers 3 (CV1 and CV3) and 5 (CV2). The electrocatalytic layers, each covered by one CV, are indicated in this figure by black vertical bars. The electrode interfaces are thus described in a discrete manner. A single CV represents the anode and the cathode catalytic layers. We are then dealing with a possible dual-porosity of the electrode region and agglomerated catalyst particles, through the use of average variables in the region. The variables are created as Gibbs excess properties.[11]

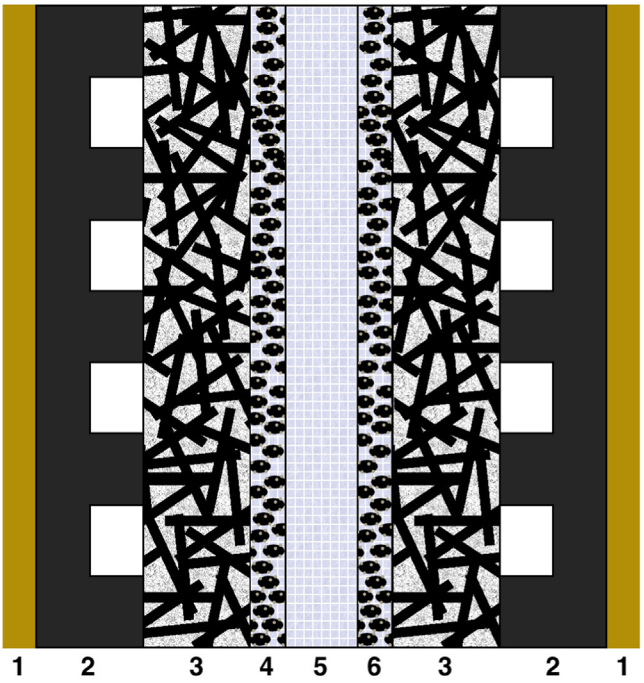

Figure 1. Cross-section of the fuel cell core, schematically. The gases in the flow fields (2) have access to the nanoporous catalyst (4 and 6) on both sides of the membrane (5) via the micro-porous layers (3) or porous transport layers (PTL).

The electrode layers have a finite thickness, but this is integrated out. This averaging procedure projects all densities of mass, energy or entropy, on to a single control volume, see right-hand side of Fig. 2, in essence, an area.

We can do this since the electrode regions are relatively thin compared to the membrane. The electrode surface in the description sketched in Fig. 2, is with this procedure regarded as an independent thermodynamic system with, say, its own temperature and excess density, say of platinum. The constitutive equations obtain a discrete form on this basis.

This way to treat the electrode layer is at variance with successful continuum models of Bernardi and Verbrugge,[8] Broka and Ekdunge,[9] and Weber and Newman.[10] It is at variance but should describe the same physical phenomena. The presented way differs from the conventional way, not only by the coarse-graining procedure for the electrode layer but also by the type of constitutive equations that are used. It also offers precise access to the entropy production of the layer(s). We describe below how these equations follow from the entropy production.

Theory

We need the entropy production to be able to define constitutive equations and give below appropriate expressions for all relevant CVs and the electrode surfaces of Fig. 2. We are seeking a simultaneous solution of the constitutive equations and the corresponding conservation equations, for all five layers.

The entropy balance.—The entropy production is standardly obtained in non-equilibrium thermodynamics by introducing mass- and energy-balances (see below) into Gibbs equation.[11]

For a control volume in a homogeneous phase, the entropy produced per m^3 is denoted σ. The total entropy production of the CV, dS_{irr}/dt, in W/K can be obtained in two ways. We can integrate σ across the CV, V. Alternatively, if we consider the system as a black box, we can find the total entropy production as the net entropy flow to the surroundings. For a 1D-system with a cross-sectional area $\Omega = 1\ m^2$, we integrate along the $x-$axis. At steady state, the

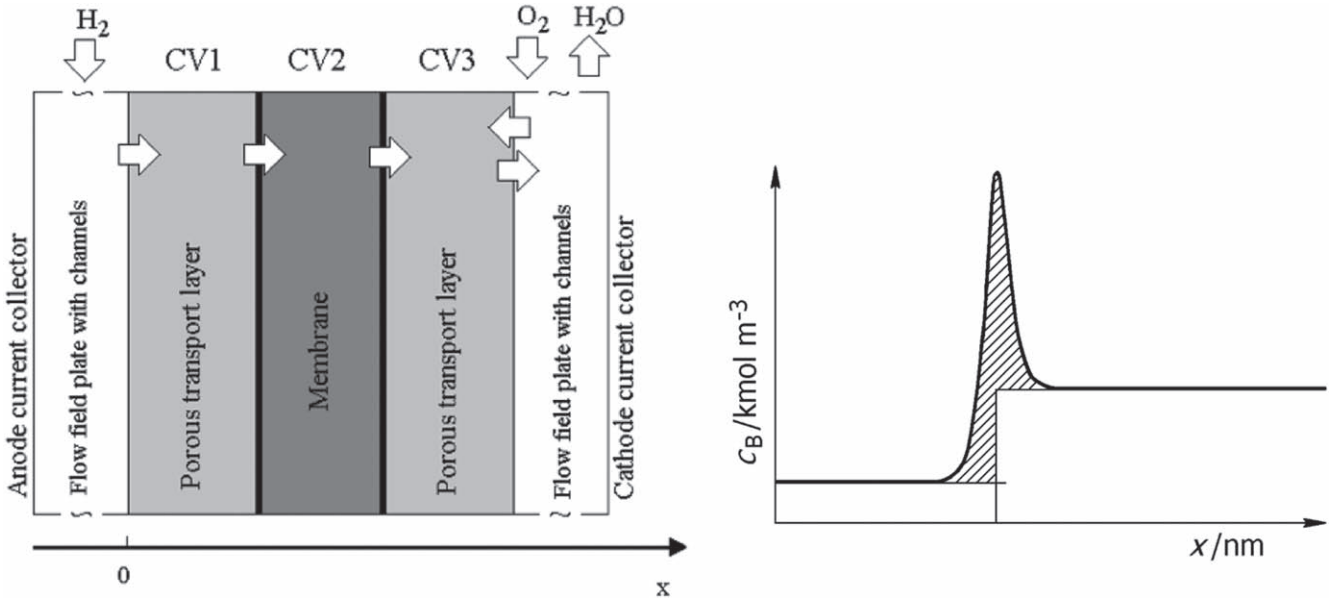

Figure 2. PEMFC layer structure (left), with an example of how to construct a surface excess density for the catalytic layer (right). The regions CV1, CV2 and CV3 indicate the continuous phases, of layers 3 and 5 in Fig. 1, while the electrocatalytic layers (4 and 6 in Fig. 1) are covered by one CV (black vertical bar). The average density in the interface, say of Pt or Nafion ionomer, is computed from the hatched area under the density variation curve on the right-hand side. The densities of layers 4 and 6 become singularities in the description of these layers. The flow fields and the current collectors are not considered here.

first and second procedures give as entropy balance:

$$\frac{dS_{irr}}{dt} = \int \sigma dV = \Omega \int \sigma dx = \Omega(J_s^{\text{out}} - J_s^{\text{in}}) > 0 \qquad [1]$$

Here J_s^{out} and J_s^{in} are the entropy fluxes out of and into the (sub-) system, respectively. We can find the entropy production from the right-hand side of the equation or from the integral. We can do this for a single layer or the whole cell. When the two numbers are the same, the thermodynamic model in use is consistent. We shall systematically use the entropy balance in this manner to check for consistency of the models we examine. The value will be computed in two ways, and the results will be compared.

The corresponding formula for the porous electrode, treated as a Gibbs surface layer, concerns the excess entropy production. The discrete form of the entropy balance at the surface is here

$$\frac{dS_{irr}^{\text{s}}}{dt} = \Omega\sigma^s = \Omega(J^{\text{s,out}} - J^{\text{s,in}}) > 0 \qquad [2]$$

Superscript s refers to the surface position. The σ^s has the unit W/K m^2 in the discrete description. Once the entropy production is derived, the constitutive equations follow, cf. (Eqs. 7 to 20).

Conservation of mass and energy.—The present analysis deals with an adiabatic 1D-fuel cell in steady state. The conservation equations for mass are, therefore, all related to the electric current density j.

$$J_{\text{H}_2} = j/2F \qquad [3]$$

$$J_{\text{O}_2} = -j/4F \qquad [4]$$

$$J_w^{\text{c}} = J_w^{\text{a}} + j/2F \qquad [5]$$

The symbol J will always be used for a flux in mol/(m^2 s), while j is the electric current density as measured in the external circuit in A m^{-2} and F is Faraday's constant in C mol^{-1}. Subscripts indicate components, hydrogen, oxygen, or water (w). Superscripts denote the homogeneous phase we are in, where a indicates the anode PTL, m the membrane and c the cathode PTL.

As we move from left to right across the cell, there is energy conversion by cell internal energy (enthalpy) and entropy into electric energy. The energy flux along the x-axis, J_u, is constant in the steady-state. For the three homogeneous phases, it takes the form[11,12]:

$$J_u = J_q'^{\text{a}} + J_{\text{H}_2}H_{\text{H}_2} + J_w^{\text{a}}H_w^{\text{a}} + j\phi^{\text{a}} \qquad [6a]$$

$$= J_q'^{\text{m}} + J_w^{\text{m}}H_w^{\text{m}} + j\phi^{\text{m}} \qquad [6b]$$

$$= J_q'^{\text{c}} + J_{\text{O}_2}H_{\text{O}_2} + J_w^{\text{c}}H_w^{\text{c}} + j\phi^{\text{c}} \qquad [6c]$$

Subscript q refers to heat, and J_q' is the measurable heat flux, while H_i is the enthalpy of component i. The potential, generated by the fuel cell reaction, between the terminals is $\phi^{\text{cell}} = \phi^{\text{c,rb}} - \phi^{\text{a,lb}}$, where rb and lb are the right and left system boundaries. The potential drop on the left-hand side (anode) is $\phi^{\text{m,a}} - \phi^{\text{a,m}}$, while at the drop on the right-hand side (cathode) is $\phi^{\text{c,m}} - \phi^{\text{m,c}}$. Superscripts indicate first the phase we are in (first symbol), and next, the neighbouring phase. The enthalpy, as well as the electric potential, are not absolute and needs a reference.

Constitutive equations for homogeneous phases.—The entropy production in any control volume is the product sum of the independent fluxes and forces.[11,13] The entropy production of a CV in the continous form, say, for the polymer membrane is:

$$\sigma = J_q'\nabla\frac{1}{T} - J_w\frac{1}{T}\nabla\mu_{w,T} - j\frac{1}{T}\nabla\phi \qquad [7]$$

Each term represents dissipation of energy as heat into the surroundings. However, each term is linked to the other terms by linear flux-force relationships. For instance, the electric potential gradient is a function not only of the current density like in Ohm's law but also of the gradient in the inverse temperature and of the chemical potential. The proportionality coefficients are the so-called Onsager coefficients, and these can be directly related to commonly used transport coefficients. We have skipped this derivation, as it can be found in the literature.[11,12] Only the matrix of Onsager coefficients is symmetric. After introducing the common coefficients, we

obtain, e.g., for the membrane:

$$\frac{dT}{dx} = -\frac{1}{\lambda^{\mathrm{m}}} J_q' + \frac{q^{*,\mathrm{m}}}{\lambda^{\mathrm{m}}}\left(J_w - t_w^{\mathrm{m}}\frac{j}{F}\right) + \frac{\pi^{\mathrm{m}}}{\lambda^{\mathrm{m}}}\frac{j}{F} \quad [8]$$

$$\frac{dx_w}{dx} = -\frac{q^{*,\mathrm{m}} x_w}{RT^2}\frac{dT}{dx} - \frac{1}{cD_w^{\mathrm{m}}}\left[J_w - t_w^{\mathrm{m}}\frac{j}{F}\right] \quad [9]$$

$$\frac{d\phi}{dx} = -\frac{\pi^{\mathrm{m}}}{TF}\frac{dT}{dx} - \frac{t_w^{\mathrm{m}} RT}{Fx_w}\frac{dx_w}{dx} - r^{\mathrm{m}} j \quad [10]$$

As usual, T is the absolute temperature in K, x_w is the water molar fraction, c is the total concentration in mol m^{-3}, ϕ is the electric potential in V, λ^{m} is the membrane thermal conductivity in W m^{-1} K, $q^{*,\mathrm{m}}$ is the heat of transfer of water in the membrane in J mol^{-1}, D_w^{m} is the diffusivity coefficient of water in the membrane in m^2 s^{-1}, t_w is the transference coefficient of water (the electro-osmotic drag coefficient), π^{m} is the membrane Peltier heat in J, and r^{m} is the membrane electric resistance in Ohm m. To convert the chemical potential gradient in Eq. 7 into the concentration gradient in Eq. 9, we used the following thermodynamic expression:

$$\mu_{w,T} = \mu_{w,T}^0 + RT\ln\left(\frac{x_w}{x_w^*}\right) \quad [11]$$

where $\mu_{w,T}^0$ is the chemical potential at constant temperature and standard conditions, and x_w^* is the water molar fraction at saturation.

The terms that are usually encountered in fuel cell modelling are the terms related to thermal conductivity (Fourier's law), diffusion (Fick's law), electric resistance (Ohm's law) and the electro-osmotic effect, represented by the water transference coefficient

$$t_w^{\mathrm{i}} = \left(\frac{J_w^{\mathrm{i}}}{j/F}\right)_{\Delta\mu_w=0} \quad [12]$$

This work has a focus on Seebeck/Peltier and Soret/Dufour effects. The Peltier coefficient of a conductor i expresses the heat reversibly carried by the electric current and is defined by

$$\pi^{\mathrm{i}} = \left(\frac{J_q'^{\mathrm{i}}}{j/F}\right)_{dT=0} \quad [13]$$

The Dufour effect expresses the heat, reversibly carried by mass fluxes (in the absence of electric current), and can be expressed by the heat of transfer. The heat of transfer is defined by

$$q^{*,\mathrm{i}} = \left(\frac{J_q'^{\mathrm{i}}}{J_w}\right)_{j=0,dT=0} \quad [14]$$

The only component free to diffuse is water. The Dufour effect can also be related to the thermal diffusion coefficient. For further details, see Refs. 11, 12. While the Peltier effect is sometimes estimated,[10] the Dufour effect has not been included in a systematic analysis as far as we know. It is the purpose of this paper to show that neither of these effects can be neglected. We see from Eq. 8 that a temperature gradient arises for several reasons. There is not only a term due to the measurable heat flux but also terms containing the Dufour and Peltier effects. Any net flux of water will carry heat in the form of a heat of transfer, while proton transfer is accompanied by Peltier heat.

The water concentration gradient in Eq. 9 is likewise a function of the electric current density, j, and of water flux, J_w, but also of the temperature gradient. The electric work, described by Eq. 10, include work done first to move heat against a temperature gradient, and second to move water against its chemical potential gradient. Finally, there is an ohmic potential drop. The work to move water against its chemical potential gradient has been neglected in the literature so far.

We have here given the set for the membrane. Similar coupled sets of constitutive equations apply to the anode and cathode PTL, see Ref. 11. Here, we use J_D, the interdiffusion flux, instead of J_w, because more then one component is present in the PTLs.

$$J_D = \left(\frac{J_w}{x_w} - \frac{J_i}{x_i}\right)x_w \quad [15]$$

where i is either hydrogen in the anode PTL or oxygen in the cathode PTL.

Constitutive equations for the electrode surfaces.—For the electrode surfaces, the entropy production has in the outset five terms, two for the transport of heat into and out of the surface, one for the transport of water across the surface, one term for the chemical reaction supplied by the gas flux, and one for the electric potential drop across the surface. For the anode side, we obtain:

$$\sigma^{\mathrm{s}} = J_q'^{\mathrm{a,m}}\left(\frac{1}{T^{\mathrm{s}}} - \frac{1}{T^{\mathrm{a,m}}}\right) + J_q'^{\mathrm{m,a}}\left(\frac{1}{T^{\mathrm{m,a}}} - \frac{1}{T^{\mathrm{s}}}\right) + J_w^{\mathrm{m,a}}\left(-\frac{\mu_w^{\mathrm{m,a}} - \mu_w^{\mathrm{a,m}}}{T^{\mathrm{m,a}}}\right) - j\left[\frac{\phi^{\mathrm{m,a}} - \phi^{\mathrm{a,m}}}{T^{\mathrm{s}}} + \frac{\Delta_n G^{\mathrm{s}}/F}{T^{\mathrm{s}}}\right] \quad [16]$$

The entropy production for the cathode surface is similar. All symbols will then refer accordingly to the cathode.

It is common in literature to assume water equilibrium across the surfaces[22]:

$$\Delta_{\mathrm{a,m}}\mu_w = 0 \quad \text{and} \quad \Delta_{\mathrm{m,c}}\mu_w = 0 \quad [17]$$

The assumption will be discussed below. Equation 17 removes the water term in the entropy production. We have also assumed equilibrium for adsorption of hydrogen (oxygen) at the anode (cathode) surface. When these conditions are combined with the above, we obtain an entropy production with three terms, and three constitutive equations (Eqs. 18, 19 and 20), for details, see Refs. 11–13.

Two subscripts separated by a comma, as in a,s, mean from phase a to phase s, where a is the anode PTL and m is the membrane and s is the electrode surface. The constitutive equations for the anode become:

$$\Delta_{\mathrm{a,s}}T = -\frac{1}{\lambda^{\mathrm{s,a}}}\left[J_q'^{\mathrm{a,m}} - q^{*,\mathrm{a}}\left(J_w^{\mathrm{a,m}} - t_w^{\mathrm{a}}\frac{j}{F}\right) - \pi^{\mathrm{a}}\frac{j}{F}\right] \quad [18]$$

$$\Delta_{\mathrm{s,m}}T = -\frac{1}{\lambda^{\mathrm{s,m}}}\left[J_q'^{\mathrm{m,c}} - q^{*,\mathrm{m}}\left(J_w^{\mathrm{m,c}} - t_w^{\mathrm{m}}\frac{j}{F}\right) + \pi^{\mathrm{m}}\frac{j}{F}\right] \quad [19]$$

$$\Delta_{\mathrm{a,m}}\phi_{\mathrm{eff}} = -\frac{\pi^{\mathrm{a}}}{T^{\mathrm{a,m}}}\frac{\Delta_{\mathrm{a,s}}T}{F} - \frac{\pi^{\mathrm{m}}}{T^{\mathrm{m,a}}}\frac{\Delta_{\mathrm{s,m}}T}{F} - r^{\mathrm{s,a}} j \quad [20]$$

$\Delta_{\mathrm{a,m}}\phi_{eff}$ is the effective electric potential at the anode, $\Delta_{\mathrm{a,m}}\phi_{eff} = \Delta_{\mathrm{a,m}}\phi + \Delta_n G^{\mathrm{s}}/F$. When $\sigma^{\mathrm{s}} = 0$ (open-circuit potential) all terms are zero. From the last term on the right-hand side in Eq. 16, we obtain the Nernst equation. The contributions to the equations are of the same type as described for the membrane. It is an advantage to know the full set of equations, Eqs. 16–20, when we want to introduce further assumptions. Surface resistances are, in general, substantial and cannot be neglected.[23] The gain by going to this level of complication in the description must be recovered in the outcome. The outcome here is a set of simultaneous variable profiles, consistent with the second law of thermodynamics.

The heat flux into a surface may differ from the heat flux out of the surface, e.g., due to changes in latent heat (see the energy balances in Eq. 6). In the present 1-D model, the fluxes of water and electric charge (protons) in the membrane are constant. The energy flux is also constant in the steady-state. This simplifies the numerical solution procedure of the equations presented.

Case Studies

In order to answer the questions raised, we implemented the model described, as shown above. We present that as a Base Case below. In Study 1, we gave the contributions from the Soret/Dufour and Seebeck/Peltier effects to the heat and water fluxes, and the electrode temperature jumps. In Study 2, we described the effect of asymmetric temperature boundary conditions. Experimental data and estimated transport properties, used to solve the equations, are given in Table I. The transport coefficients used in our model are effective coefficients. For the surface, they refer to the whole surface area and are excess properties. For the homogenous layers/the continuous description, we use local coefficients. For instance, the electric resistance is a function of temperature and water content in the membrane, but a constant at the surface or PTL.

Base case.—The Base Case presents all relevant profiles with equilibrium and transport properties as defined in Table I, and below.

Study 1. Peltier and Dufour effects.—Coupling terms, like the Soret/Dufour and Seebeck/Peltier effect, in the Base Case were computed, to study the impact of these effects on temperature jumps, heat and water fluxes, as a function of current density.

Study 2. Thermal boundary conditions.—In the second study, we investigated the influence of different boundary temperatures compared to the Base Case. The temperatures at both sides varied, as shown in Table III. The main questions were: How does the PEMFC respond to temperatures change on the boundaries? What are the practical implications of the findings?

Solution Procedures

All computations were performed in MATLAB R2019a. The code was based on the published open-source code of Vetter and Schumacher.[20] This utilised the bvp4c solver to solve a multi-point boundary value problem. The differences between our implementation and the code[20] were:

(i) Equations presented in the theory replaced the differential equations of Vetter and Schumacher.[20]
(ii) The parameter sweep was done by changing the current density instead of the voltage.
(iii) Three domains were used for the multi-point boundary value problem instead of five. The domains were the anode PTL, the membrane and the cathode PTL.
(iv) The equations for the electrodes were solved in the boundary condition function. This was needed in the bvp4c solver and then included in the boundary conditions. With this, it was possible to model the electrodes as surfaces without a spatial discretisation, which is an advantage in our set-up.
(v) The Butler-Volmer equation (Eq. 21) was solved iteratively with MATLAB's build-in fzero algorithm.

Table I. Transport coefficient values used for the Base Case and further studies in this investigation.

Parameter	Unit	Value
r^{m}	ohm m	calculated[24]
$r^{a} = r^{c}$	ohm m	2.1×10^{-4} [25]
$r^{s,a} = r^{s,c}$	ohm m^2	7.2×10^{-6} [11]
λ^{m}	W Km^{-1}	calculated[26]
$\lambda^{a} = \lambda^{c}$	W Km^{-1}	0.38[25]
$\lambda^{s,a} = \lambda^{s,m} = \lambda^{s,c}$	W Km^{-2}	1000[11]
$D^{a}_{wH_2}$, $D^{c}_{wO_2}$, D^{m}_{w}	m^2 s^{-1}	calculated[24,27]
$l^{a} = l^{c}$	m	235×10^{-6} [25]
l^{m}	m	50.8×10^{-6} [28]
j_0	A m^{-2}	calculated[29]
$q^{*,m}$	J mol^{-1}	$-TS_w$ [11,30]
t^{m}_{w}	mol w mol^{-1} H+	1.2[11]
$t^{a}_{w} = t^{c}_{w}$	mol w mol^{-1} H+	0[11]

Figure 3 shows the schematic of the numerical solving process of this model. First the boundary conditions and parameters were set. Based on the first current density value, the initial guess was computed. Inside the bvp4c solver, each layer was solved and the

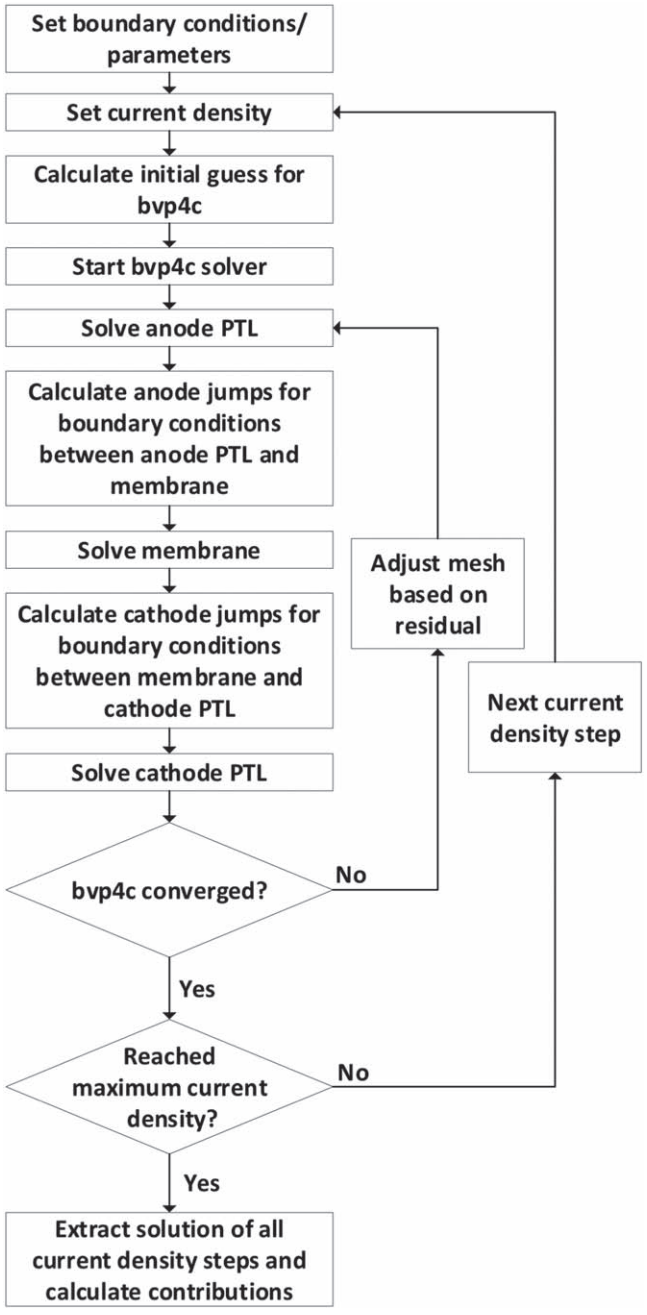

Figure 3. Schematic of the numerical solving process of the model.

boundary conditions between the anode PTL and membrane and the membrane and cathode PTL were computed from the jumps on the electrode surfaces. If the solution converged, the next current density step was chosen and the process of solving the differential equations started again. In the end the solution of all current density steps is extracted and contributions to heat and water flux and to the temperature jumps at the electrodes are calculated. As convergence criteria we set a relative error tolerance of 10^{-4} and an absolute error tolerance of 10^{-6} in the bvp4c solver, which was the reference value in the open-source code from Vetter and Schumacher.[20]

The Butler-Volmer equation, used for both electrodes, included a correction from the partial fuel pressure at the electrodes[21]:

$$j = j_0\left[\exp\left(\frac{\alpha n F\eta}{RT}\right) - \exp\left(\frac{-(1-\alpha)nF\eta}{RT}\right)\right] \quad [21]$$

Here η is the overpotential in V, α is the charge transfer coefficient of the electrode, n is the number of electrons involved in the cell reaction, which was $n = 2$ in our case. α was set to 0.5. The exchange current density j_0 of Eq. 21 was adjusted to depend on the ratio of the actual and standard gas pressure at the electrode.[29] j_0 got replaced by either j_{0,O_2} or j_{0,H_2} depending on the electrode.

$$j_{0,O_2} = \mathrm{EPSA^c}\, j'_{0,O_2}\left(\frac{p_{O_2}}{p^0}\right)^{0.001678T} \quad [22]$$

$$j_{0,H_2} = \mathrm{EPSA^a}\, j'_{0,H_2}\left(\frac{p_{H_2}}{p^0}\right)^{0.5} \quad [23]$$

Here j_{0,O_2} and j_{0,H_2} are the revised equilibrium exchange current densities for oxygen (cathode) and hydrogen (anode) respectively in A m^{-2}, EPSA is the electrochemical Pt surface area of the cathode or anode in the unit of cm^2 Pt surface per cm^2 electrode geometric area (cm^2/cm^2), j'_{0,O_2} and j'_{0,H_2} are the intrinsic exchange current densities in A m^{-2} of the cathode and anode, p_{O_2} and p_{H_2} are partial pressures of oxygen and hydrogen, respectively, p^0 is the standard pressure in bar, and T is the temperature at the cathode surface. The values for the intrinsic exchange current densities, $j'_{0,O_2} = 3 \times 10^{-5}$ A m^{-2} and $j'_{0,H_2} = 10$ A m^{-2}, were taken from Ref. 21.

The EPSA was calculated with the following equations[29]:

$$\mathrm{EPSA^c} = 0.02396T'^2 - 5.958 * T' + 429.3 \quad [24]$$

$$\mathrm{EPSA^a} = 0.0009915 * T'^2 - 0.5201 * T' + 55.94 \quad [25]$$

where T' is the temperature at the anode or cathode in degrees Celsius.

The boundary conditions of the cell domains are given in Tables II and III, where a denotes the anode PTL, m the membrane, c the cathode PTL, lb the left and rb the right boundary of the PEMFC. The temperature T and water molar fraction x_w had a fixed value on both the left and right boundary of the fuel cell. x_w on the outer boundaries was calculated based from saturation pressure at a given temperature and the set relative humidity.[31] The potential ϕ and entropy production σ were set to zero on the left inlet. The electrode reactions at the interfaces between the different domains, give jumps in the boundary conditions there. We added a term for each variable, calculated from Eqs. 18 and 20. Using Eq. 17 we obtained the water activity at the entrance of the membrane, a_w^{entrance} and the water activity at the entrance of the cathode PTL (left side of cathode PTL), x_w^{entrance} in Eqs. 26 and 27. Equations 26 and 27 were then used as boundary conditions, see Table II.

$$\ln a_w^{\mathrm{entrance}} = \frac{\mu_w^{\mathrm{m,a}} - H_w^{\mathrm{m,a}}}{RT^{\mathrm{m,a}}} + S_w^{0,\mathrm{m}} + \frac{c_{p,w}^{\mathrm{m}}}{R}\ln\left(\frac{298}{T^{\mathrm{m,a}}}\right) \quad [26]$$

where $\mu_w^{\mathrm{m,a}}$ is the chemical potential at the left side of the membrane, which is, due to the equilibrium assumption, $\mu_w^{\mathrm{m,a}} = \mu_w^{\mathrm{a,m}} = H_w^{\mathrm{a,m}} - T^{\mathrm{a,m}}S_w^{\mathrm{a,m}}$, $H_w^{\mathrm{m,a}}$ is the enthalpy of liquid water on the left side in the membrane, $S_w^{0,\mathrm{m}}$ is the standard entropy of liquid water and $c_{p,w}^{\mathrm{m}}$ is the specific heat capacity of liquid water in the membrane.

$$\ln x_w^{\mathrm{entrance}} = \frac{\mu_w^{\mathrm{c,m}} - H_w^{\mathrm{c,m}}}{RT^{\mathrm{c,m}}} + S_w^{0,\mathrm{c}} + \frac{c_{p,w}^{\mathrm{c}}}{R}\ln\left(\frac{298}{T^{\mathrm{c,m}}}\right) \quad [27]$$

where $\mu_w^{\mathrm{c,m}}$ is the chemical potential at the left side of the cathode PTL, which is, due to the equilibrium assumption, $\mu_w^{\mathrm{c,m}} = \mu_w^{\mathrm{m,c}} = H_w^{\mathrm{m,c}} - T^{\mathrm{m,c}}S_w^{\mathrm{m,c}}$, $H_w^{\mathrm{c,m}}$ is the enthalpy of vapor water on the left side in the cathode PTL, $S_w^{0,\mathrm{c}}$ is the standard entropy of vapor water and $c_{p,w}^{\mathrm{c}}$ is the specific heat capacity of vapor water in the cathode PTL.

Schroeder's paradox describes that the membrane water content λ_w depends on the state of the neighbouring phase in equilibrium with the membrane. With water vapor in contact with the membrane, as was the case here, the water activity cannot go above 1, and the water content upper limit is (approximately) 14 molecules per membrane ionic site. Therefore we used the data of Weber and Newman.[32] A curve fit was done on the data from Weber and Newman, resulting in Eq. 28.

$$\lambda_w = 1.07e - 14e^{34.2a_w} + 1.4e^{1.96a_w} \quad [28]$$

The numerical solutions were found for current densities between 0 and 14000 A m^{-2}. These current densities cover the normal range of cell operation. The electric current density was constant through the cell, while the measurable heat flux and the water flux were jumping at the interfaces, due to phase transitions of water and due to the production of water. These fluxes and the resulting profiles were calculated as described below.

The Base Case and Study 1 used boundary temperatures of 340 K and a relative humidity of 70% at both sides of the fuel cell and a constant pressure of 1.013 bar.

The contributions to the water and heat fluxes and the temperature jumps at the electrodes were calculated, using the results of the integration across the whole cell for all current densities. The temperature boundary conditions in Study 2 are given in Table III. Again a pressure of 1.013 bar and a relative humidity of 70% was used.

Results and Discussion

Base case.—The results of the Base Case are plotted in Figs. 4, 5 and 6, and discussed in the following.

Table II. Boundary conditions of the different domains in the boundary value problem. The superscript's first letter describes the homogeneous layer and the second letter describes the position. This can either be on the left or right side of the layer, indicated by the second letter of the superscript, which denounces the neighbouring phase. Superscripts lb and rb stand for left and right boundary at the inlets of the fuel cell.

	Inlet left | a PTL	a PTL | m	m | c PTL	c PTL | Inlet right
T	$T^{\mathrm{a,lb}} = T^{\mathrm{lb}}$	$T^{\mathrm{m,a}} = T^{\mathrm{a,m}} + \Delta_{\mathrm{a,m}}T;\ J_q'^{\mathrm{m,a}} = J_q'^{\mathrm{a,m}} + \Delta_{\mathrm{a,m}}J_q'$	$T^{\mathrm{c,m}} = T^{\mathrm{m,c}} + \Delta_{\mathrm{m,c}}T;\ J_q'^{\mathrm{c,m}} = J_q'^{\mathrm{m,c}} + \Delta_{\mathrm{m,c}}J_q'$	$T^{\mathrm{c,rb}} = T^{\mathrm{rb}}$
x_w	$x_w^{\mathrm{a,lb}} = x_w^{\mathrm{lb}}$	$J_w^{\mathrm{m,a}} = J_w^{\mathrm{a,m}} + \Delta_{\mathrm{a,m}}J_w$	$x_w^{\mathrm{c,m}} = x_w^{\mathrm{entrance}};\ J_w^{\mathrm{c,m}} = J_w^{\mathrm{m,c}} + \Delta_{\mathrm{m,c}}J_w$	$x_w^{\mathrm{c,rb}} = x_w^{\mathrm{rb}}$
ϕ	$\phi^{\mathrm{a,lb}} = 0$	$\phi^{\mathrm{m,a}} = \phi^{\mathrm{a,m}} + \Delta_{\mathrm{a,m}}\phi$	$\phi^{\mathrm{c,m}} = \phi^{\mathrm{m,c}} + \Delta_{\mathrm{m,c}}\phi$	
σ	$\sigma^{\mathrm{a,lb}} = 0$	$\sigma^{\mathrm{m,a}} = \sigma^{\mathrm{a,m}} + \Delta_{\mathrm{a,m}}\sigma$	$\sigma^{\mathrm{c,m}} = \sigma^{\mathrm{m,c}} + \Delta_{\mathrm{m,c}}\sigma$	
a_w		$a_w^{\mathrm{m,a}} = a_w^{\mathrm{entrance}}$		

Table III. Temperatures used in the calculations at the fuel cell boundaries where T^{lb} and T^{rb} are the temperatures at the left and right boundaries of the system (inlets) in K used in Study 2.

Case	T^{lb}	T^{rb}
1	350	350
2	335	340
3	340	335
4	340	345
5	345	340

The polarization curve.—The reference (Base Case) polarization curve is plotted as a solid black line in Fig. 4 (left). Additionally, the power density curves for the different temperatures are shown in Fig. 4 (right). The curve reproduced results well known from the literature with similar conditions cf. Rahgoshay et al. (boundary temperatures of 350 K and a pressure of 1.5 bar).[33] Yuan et al.[34] showed also similar results over the mid-range of current densities; however, a higher relative humidity was used (100%). We saw the initial drop due to the cathode overpotential from the reversible limit value 1.185 V to approximately 0.85 V at 100 A m^{-2}. Even though air was used on the cathode side and the Butler-Volmer equation was utilised with a partial pressure correction, the voltage drop at high current densities was still linear in the current density. The result did not change by reducing the diffusion coefficient a factor of 10. The other lines, shown in Fig. 4, refer to Studies 1 and 2 and are discussed below.

Temperature- and heat flux profile.—Generally, we reported higher temperatures/temperature jumps in the fuel cell than known from other authors.[10,20,33] Qualitatively, a general rise of a few degrees above the boundary value has been reported. Using our equations, we can identify the cause of the profiles. We first noted that the heat flux, as pictured in Fig. 5d, was pointing out of the fuel cell at typical current densities, on both the anode and the cathode side. This is consistent with the fact that fuel cells, especially fuel cell stacks, need to be cooled during operation.[21]

The temperature profile, pictured in Fig. 5a, showed two interesting facts, a very high temperature at the cathode (349 K as compared to 340 K at the boundaries, and significant temperature jumps at both electrodes, up to 3 and 2 K above the PTL on the anode and cathode side, respectively, at around 8000 A m^{-2}). The temperature profile had its highest point at the cathode (membrane side). At lower current densities the higher temperature was on the PTL side of the cathode, whereas at higher current densities the higher temperature was on the membrane side of the cathode. Rowe and Li showed a similar profile, where the highest temperature was at the membrane/cathode interface.[35] However, no jumps at the electrode interfaces were implemented by them.

This could be explained by looking at the heat flux in the membrane, see Fig. 5d. At lower current densities, we had a positive heat flux into the membrane, which decreased and became negative at higher current densities. The heat flux had a significant influence on the temperature jump at the anode, which will be discussed further below in connection with Study 1. We shall see the explanation that the coupling terms could lead to higher temperatures and higher jumps.

The obvious reason for the jumps across the electrode surfaces was the energy released by water condensation when water goes from gaseous state in the anode PTL to liquid state in the membrane. This was reflected in the change in enthalpy in the energy balance, e.g., of the anode, cf. Eqs. 6a and 6b. Due to the phase transition, this term played a vital role in the energy balance,

$$J_q'^{a} - J_q'^{m} + j\phi^{a} - j\phi^{m} + J_{H_2}H_{H_2} + J_w^{a}H_w^{a} - J_w^{m}H_w^{m} = 0 \quad [29]$$

Vie et al.[36] observed a difference of max. 3–4 K between the left and right side of the PTLs for a wide range of current densities with a cell temperature of around 338 K at open cell voltage, but at higher pressure (4.5 bar). Results of our model showed smaller temperature differences in the anode PTL and higher ones in the cathode PTL. Our observation differs from Vie et al.'s. This could be linked to different operating conditions such as overall temperature, pressure etc.. Furthermore, in a 1D model, heat can only leave in the x-direction, while in reality, heat also leaks to the other sides. The measurements will, therefore, give smaller differences.

Water and water flux profile.—The water concentration profile and water flux at the anode and cathode sides as well as in the membrane were well studied in the literature. The results for the cathode PTL fitted well with the ones from Vetter and Schumacher.[20] In the anode PTL, we observed the opposite gradient in the water molar fraction profile for very high current densities. However, the model only accounts for water vapor. The gradient in the water mole fraction varied largely with the current density, see Fig. 5b. Water was always transported out of the cathode region, in agreement with the production of water (Eq. 5).

The water activity in the membrane did not exceed unity in the model, even at the highest current density, in agreement with the

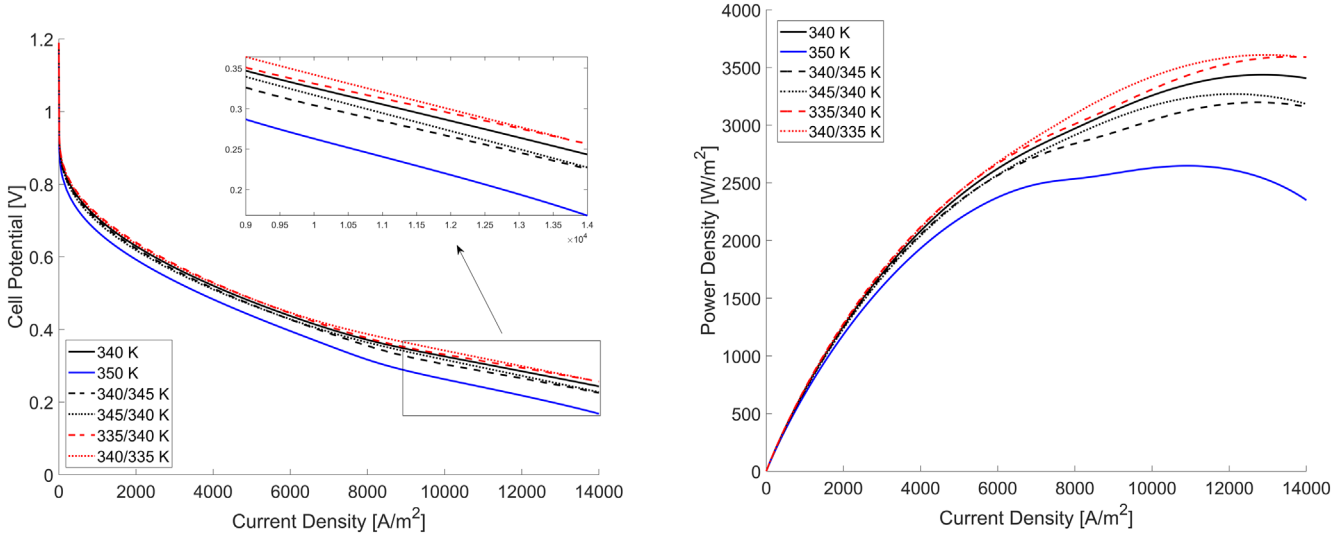

Figure 4. IV curves (left) and power density curves (right) at 1.013 bar and 70% relative humidity at different temperatures at the outer boundaries of the cell.

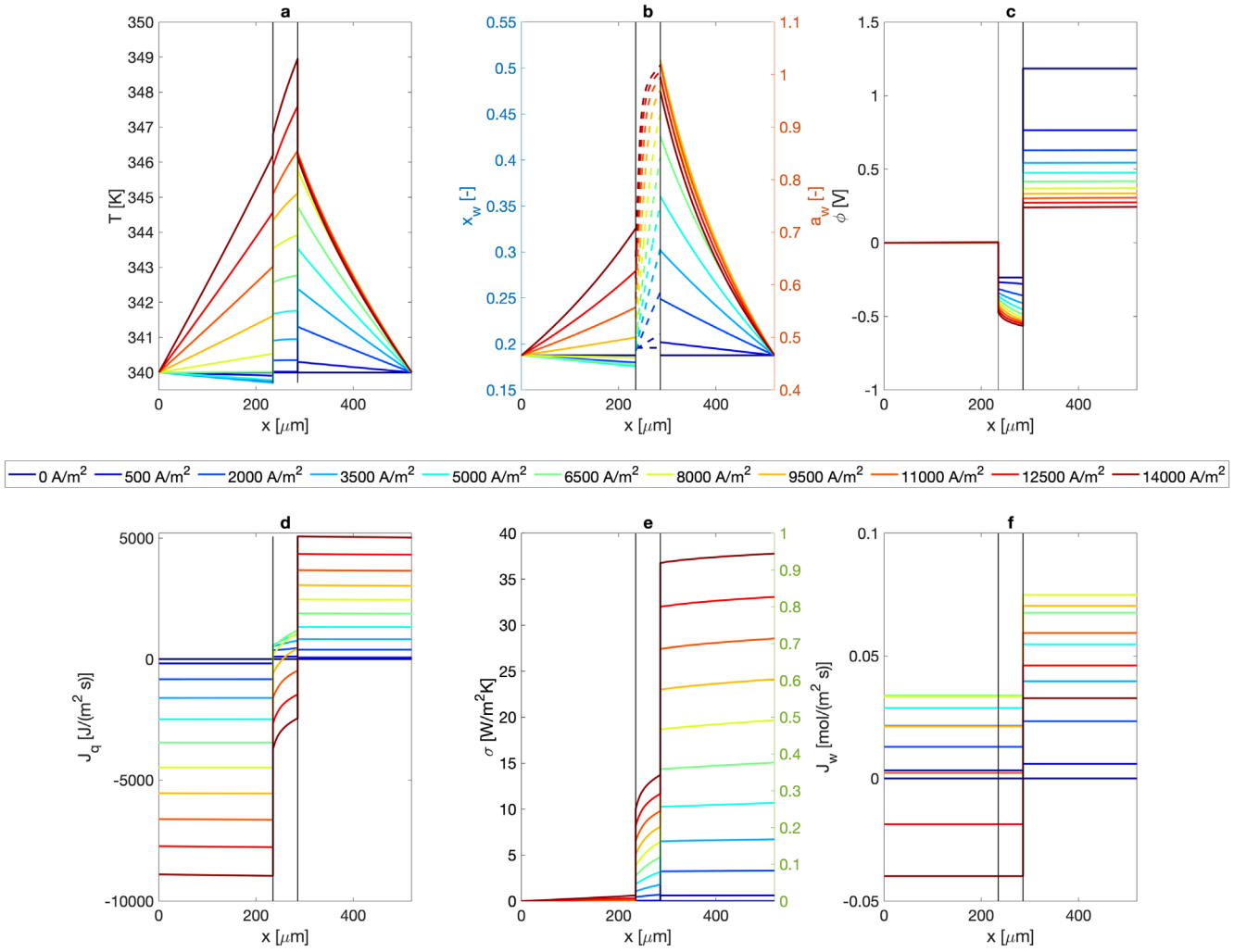

Figure 5. Profiles of Base Case at 340 K and 70% relative humidity at both outer boundaries at 1.013 bar constant pressure.(a) Temperature profile in K, (b) water molar fraction and activity profile, (c) potential profile in V, (d) measurable heat flux profile in J/(m^2 s), (e) entropy production profile in W/(m^2 K) and (f) water flux profile in mol/(m^2 s).

Weber and Newman water isotherm[32] and Schroeder's paradox. We saw at higher current densities that the membrane became more and more saturated with water.

Water was transported from the anode to the cathode for most current densities. At $j = 11000$ A m^{-2} there was, however, a sign change in the gradient of the mole fraction (cf. Fig. 5b), reflecting a change in the direction of the membrane water flux, see Fig. 5f. This information was not visible from Fig. 5b alone. It followed from the expression for the water flux. Weber and Newman[10] already showed that high current densities (low voltage in their case) resulted in a negative water vapor flux in the anode PTL. The highest molar fraction was, however, always at the cathode, fitting well with the fact that water was produced there. The profiles in the membrane were non-linear, for various reasons; coupling effects or the dependence of the resistance on temperature.

These points will be further discussed below, where we present the different contributions to the water flux.

Electric potential and entropy production profile.—The electric potential profile is shown as a function of current density in Fig. 5c. We set the start value to zero on the left side of the anode PTL, and the decline to the anode surface was negligible, even at high current densities, reflecting the small resistance. The anode potential drop at $j \approx 0$ was mainly due to the pressure of the hydrogen gas being different from 1.013 bar. This drop is explained by the entropy of hydrogen at the reaction site. There is also a small anode overpotential, calculated with Eq. 21.

Across the membrane, the curves show a decreasing negative slope, due to the membrane resistance and the water saturation. The figure shows a detrimental voltage drop at high current densities despite the resulting high water saturation, Fig. 5b. The increase in the potential on the cathode side gives the essential conversion of chemical to electric energy. It is essentially the overpotential (Eq. 21), the partial pressure of oxygen, that lowers the potential, increasingly more as the current density increases. Most of these features are well-known from the literature, see e.g. Refs. 9, 21, apart from the details given for the anode surface, see for instance.[20]

The accumulated entropy production reflected to a large degree the potential profile. It grew where the other was reduced. The highest entropy production was at the cathode. Therefore to minimize the overall entropy production in the system, and make the fuel cell more efficient, one should start to improve the cathode.

The entropy balance and the error in the entropy production, cf. Fig. 6, was used to systematically identify errors in the code, during the making of the model program. For instance, a wrong enthalpy value caused an unphysical singularity in the results of a single modelling domain, and could easily be excluded.

The error in the entropy production (Fig. 6 was calculated with the help of Eqs. 1 and 2). Figure 6 gives an estimate of how good the assumptions and models are. The error was in general low and

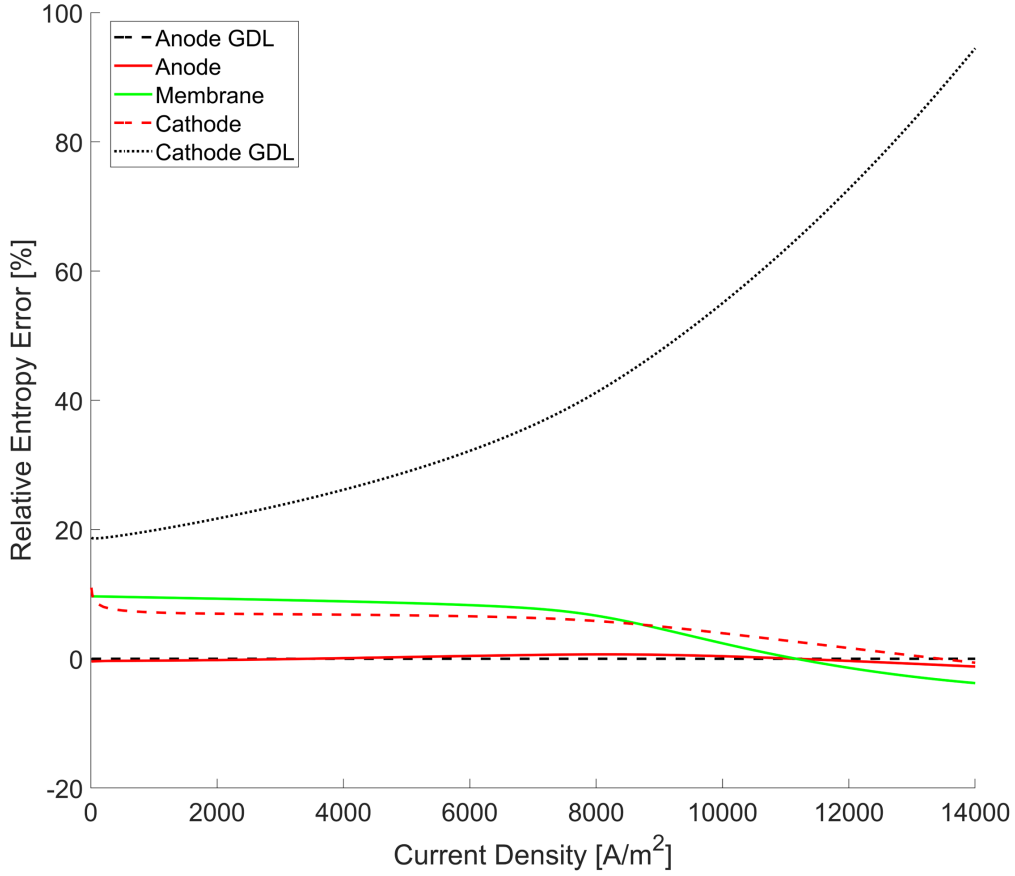

Figure 6. Overall relative entropy error of different parts of the system at varying current densities for the Base Case.

decreased with an increase in current density. This showed that there were no major flaws among our assumptions. In particular, the models for the anode and cathode surfaces seems reasonable. The cathode PTL, however, had an ever-increasing error, with a maximum of around 95%. This meant that some assumptions made for the cathode PTL were not reasonable. We suspect that they relate to the water model.

Most importantly, we can use the entropy balance to elucidate the assumptions of water equilibrium across the electrode surfaces, cf. Eq. 17. Since the entropy balance is obeyed on both the anode and cathode surfaces (low relative entropy error), the assumption is justified, or the results are consistent with our model.

Study 1.—In Study 1 we investigated the contributions to the heat and water flux, such as Soret/Dufour and Seebeck/Peltier effects, in the homogeneous phases and the temperature jumps at the electrodes to see the importance of coupling effects based on the results from the Base Case.

Contributions to the heat flux in the homogeneous phases.—The contributions to the measurable heat flux from the Fourier, Peltier and Dufour effects were of interest. The various contributions were computed from the equations shown below, at a temperature of 340 K and 70% relative humidity. Equations 30 to 32 give the contributions in the different homogenous layers to the overall heat flux J_q' were calculated.

$$J_q'^{\mathrm{a}} = -\lambda^{\mathrm{a}}\frac{dT}{dx} + q^{*,\mathrm{a}}\left(J_D - t_w^{\mathrm{a}}\frac{j}{F}\right) + \pi^{\mathrm{a}}\frac{j}{F} \qquad [30]$$

$$J_q'^{\mathrm{m}} = -\lambda^{\mathrm{m}}\frac{dT}{dx} + q^{*,\mathrm{m}}\left(J_w - t_w^{\mathrm{m}}\frac{j}{F}\right) + \pi^{\mathrm{m}}\frac{j}{F} \qquad [31]$$

$$J_q'^{\mathrm{c}} = -\lambda^{\mathrm{c}}\frac{dT}{dx} + q^{*,\mathrm{c}}\left(J_D - t_w^{\mathrm{c}}\frac{j}{F}\right) + \pi^{\mathrm{c}}\frac{j}{F} \qquad [32]$$

The first term on the right hand side in Eqs. 30 to 32 described the Fourier heat contributions to the measurable heat flux J_q'. The second term describes the Dufour contribution, and the last part is the Peltier heat. Results were computed for a location in the middle of a layer. The results were plotted as a function of current density in Fig. 7a for the anode PTL, Fig. 7b for the membrane and Fig. 7c for the cathode PTL. The graphs give a detailed background of the previous figures (cf. Fig. 5). The heat flux in each homogeneous phase varied significantly with the current density.

The figures (Fig. 7) show that there is no reason to neglect any of the contributions to the overall flux, a priori. The measurable heat flux value is shown by the solid line. We saw that the various effects differ in sign, but in all cases, we obtained a net transport of heat out of the fuel cell, as expected.

In the anode PTL, the heat flux out of the cell was mainly due to Fourier and Dufour effects. In the membrane, the heat flux changed sign. It started with a small positive value, caused by the Peltier term. At around 9700 A m^{-2}, it became negative. The cathode surface temperature gave then rise to a Fourier term, which again led to a heat loss from the cell also out through the anode PTL. The Peltier heat (or the corresponding entropy flux) was a significant contribution to this in both PTLs.

In the cathode PTL we had a low measurable heat flux, lower than that reported by Vetter and Schumacher.[20] This is probably because we have included the counteracting Dufour-effect, while this was not taken along by Vetter and Schumacher.[20] The last issue applies to all results shown in Figs. 6a–6c. The Dufour effect is connected to the entropy of water, which is large.[30] These results fit well with the computations form Huerta et al.,[15] who showed that the

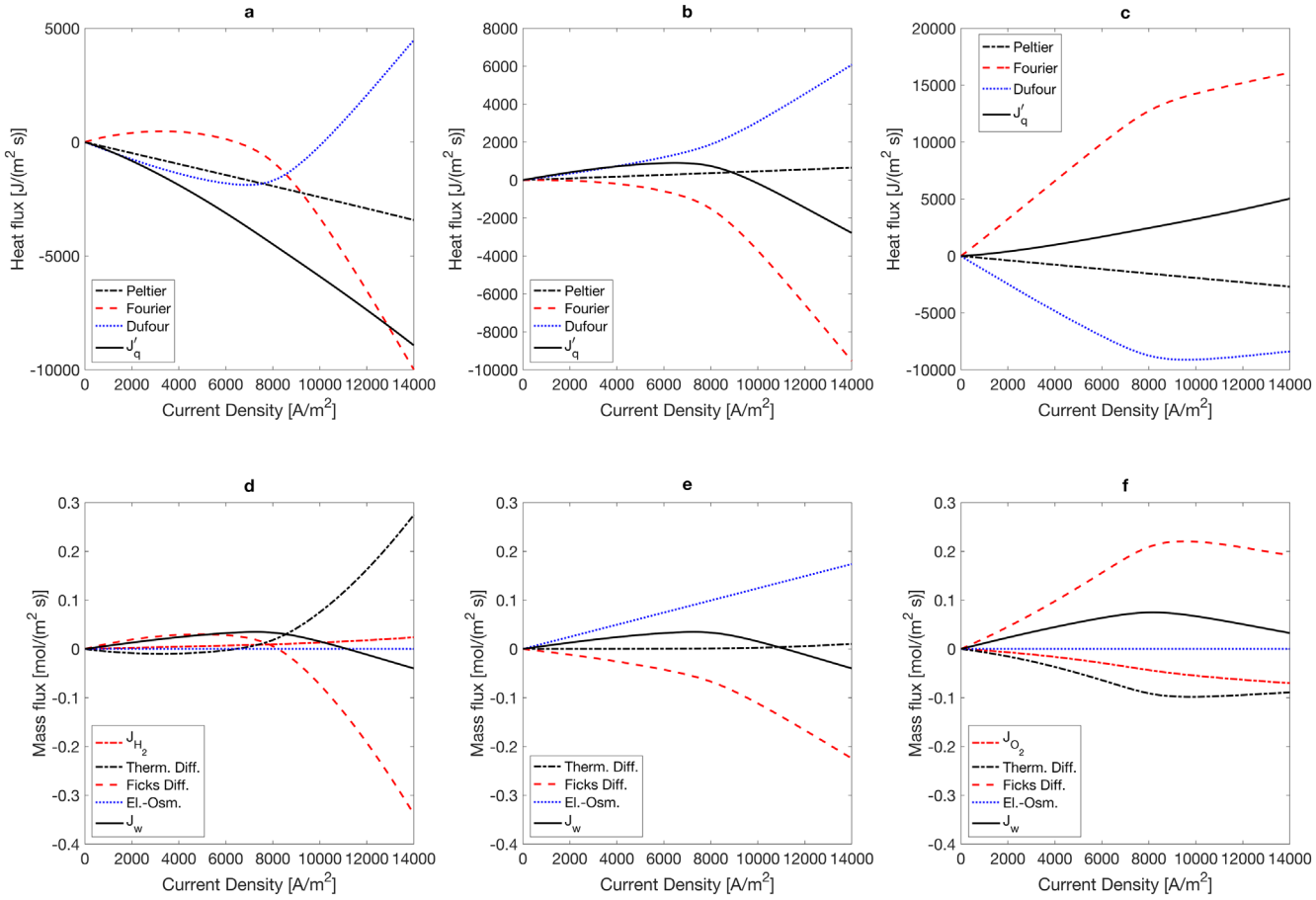

Figure 7. Contributions in J/(m^2 s) to the overall heat flux J'_q in the anode PTL (a), membrane (b) and cathode PTL (c) for different current densities. Contributions in mol/(m^2 s) to the overall water flux J_w in the anode PTL (d), membrane (e) and cathode PTL (f) for various current densities.

Peltier heat has a significant contribution to the heat fluxes in the solid oxide fuel cell.

Contributions to the temperature jumps at the electrode surfaces.—In order to compare the different contributions to the temperature jumps at the anode and cathode surfaces, we consider their analytic expressions:

$$\Delta_{\mathrm{a,m}}T = -\frac{1}{\lambda^{\mathrm{s,a}}}(J_q'^{\mathrm{a,m}} + J_q'^{\mathrm{m,a}}) + \frac{1}{\lambda^{\mathrm{s,a}}}\left(q^{*,\mathrm{a}}\left(J_w^{\mathrm{a,m}} - t_w^{\mathrm{a}}\frac{j}{F}\right) + q^{*,\mathrm{m}}\left(J_w^{\mathrm{m,a}} - t_w^{\mathrm{m}}\frac{j}{F}\right)\right) - \frac{j}{\lambda^{\mathrm{s,a}}F}(\pi^{\mathrm{a}} + \pi^{\mathrm{m}}) \quad [33]$$

$$\Delta_{\mathrm{m,c}}T = -\frac{1}{\lambda^{\mathrm{s,c}}}(J_q'^{\mathrm{m,c}} + J_q'^{\mathrm{c,m}}) + \frac{1}{\lambda^{\mathrm{s,c}}}\left(q^{*,\mathrm{m}}\left(J_w^{\mathrm{m,c}} - t_w^{\mathrm{m}}\frac{j}{F}\right) + q^{*,\mathrm{c}}\left(J_w^{\mathrm{c,m}} - t_w^{\mathrm{c}}\frac{j}{F}\right)\right) - \frac{j}{\lambda^{\mathrm{s,c}}F}(\pi^{\mathrm{m}} + \pi^{\mathrm{c}}) \quad [34]$$

The temperature jumps in the anode and cathode surfaces are plotted in Fig. 8. We identified three terms on the right-hand side in Eqs. 33 and 34:

(i) Contributions due to the effective heat flux J'_q.
(ii) Contributions due to the coupling between heat and mass (Dufour effect).
(iii) Contributions due to the coupling between heat and charge (Peltier effect).

For both the anode and cathode, the temperature change coming from the Peltier effect was sizable. Furthermore, the temperature jump caused by the Dufour effect, the coupling between the heat and mass flux, was significant. The minimum in the curve could be traced to the variation in the water flux and electro-osmotic drag term $t_w j/F$. The combination of the two terms showed a corresponding maximum in Figs. 8a and 8b. This shows the importance of coupling terms in the set of equations again. For both electrodes, we saw a change in the gradient of the temperature jump and even a sign change in the cathode. This was mainly caused by the sudden change of the contribution from the Dufour effect. The sign change was the reason why the cathode PTL side was the warmer side at low current density at the cathode, as described in the Base Case results discussion above.

Contributions to the water flux in the homogeneous phases.—Zaffou et al.[37] has pointed out that thermal diffusion needs to be reconsidered in the modelling of fuel cells. Additionally, Kim and Mench[38] measured the thermo-osmotic water flux in the membrane, showing its importance. Our results confirm these finding and show why. The contributions to the overall water flux in the anode PTL, membrane and cathode PTL are described by Eqs. 35 to 37.

$$J_w^{\mathrm{a}} = J_{\mathrm{H_2}}\frac{x_w}{1-x_w} - D_{w\mathrm{H_2}}^{\mathrm{a}}\frac{q^{*,\mathrm{a}}x_w}{RT^2}\frac{dT}{dx} - D_{w\mathrm{H_2}}^{\mathrm{a}}\frac{dx_w}{dx} + t_w^{\mathrm{a}}\frac{j}{F} \quad [35]$$

$$J_w^{\mathrm{m}} = -\frac{q^{*,\mathrm{m}}D_w^{\mathrm{m}}\lambda_w\rho}{RMT^2}\frac{dT}{dx} - \frac{D_w^{\mathrm{m}}\rho}{M}\frac{d\lambda_w}{dx} + t_w^{\mathrm{m}}\frac{j}{F} \quad [36]$$

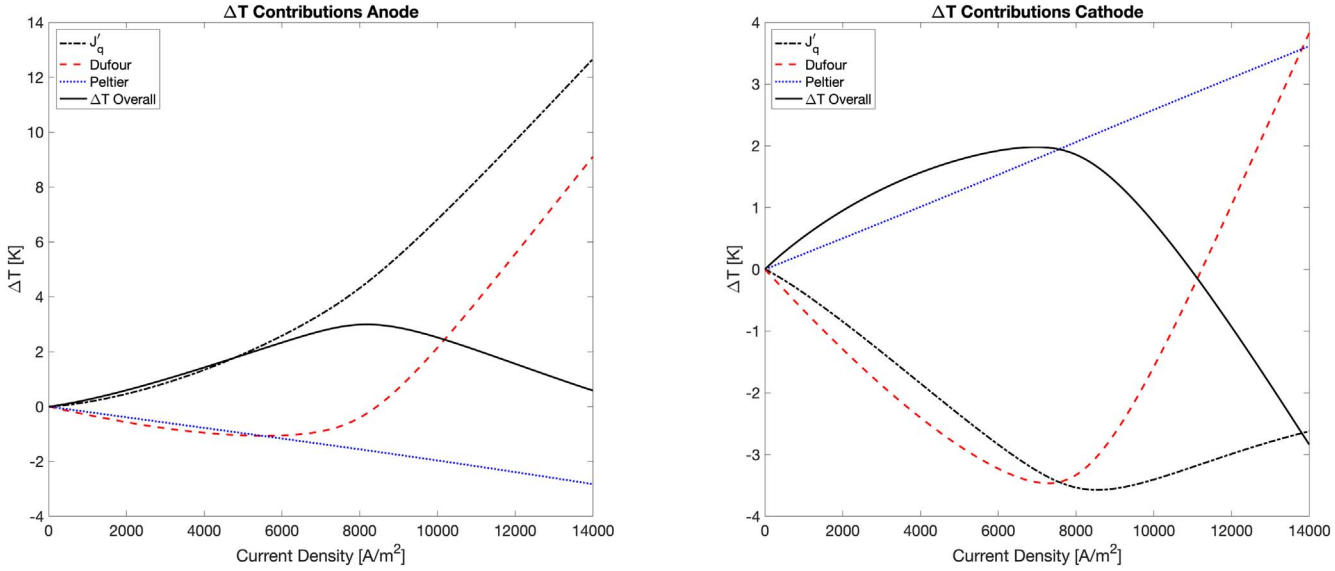

Figure 8. Contributions in K to the temperature jump at the anode (left) and cathode surface layer for different current densities.

$$J_w^c = J_{O_2}\frac{x_w}{0.21(1-x_w)} - D_{wO_2}^c\frac{q^{*,c}x_w}{RT^2}\frac{dT}{dx} - D_{wO_2}^c\frac{dx_w}{dx} + t_w^c\frac{j}{F} \quad [37]$$

Here, J_w^m is the overall water flux in mol/(m^2 s), λ_w is the water content in the membrane in mole water per mole membrane ionic site, M is the molar mass of the polymer in the membrane in kg mol^{-1} and ρ is the membrane dry density in kg m^{-3}. The first term on the right-hand side, only available in the water flux equation for the anode and cathode PTL, describes the influence of the hydrogen and oxygen flux, introduced by the interdiffusion flux J_D. The second term describes the coupling between mass and heat (thermal diffusion), the third one is the main term given by Fick's law, and the fourth term is the electro-osmotic drag. Figures 7d to 7f show how each of the contributions changed with the current density.

In the anode (Fig. 7d) and cathode PTL (Fig. 7e), we saw two counteracting effects again, but this time the effects were Fick's diffusion and thermal diffusion. This is commonly not discussed in the literature. The role played by oxygen in the cathode was significant. The competition between the diffusion of water and oxygen as given by Eq. 15 led to the profile in Fig. 5f. For both PTLs, the electro-osmotic drag contribution was zero due to t_w^a and t_w^c being zero (see Table I).

Temperature gradients can have a significant impact on the water management in the PEMFC. One reason is directly linked to the thermal diffusion in the system. Higher temperature gradients will increase the thermal diffusion. As it is shown in Fig. 7f, the contribution of the thermal diffusion decreases the overall water flux in the cathode PTL. If the temperature difference in the cathode PTL would be reduced, the thermal diffusion will reduce too. Therefore, the overall water flux increases, which should help with removal of water. On the other hand, higher temperatures are beneficial to the water management, because more water is evaporating, decreasing the risk of pore blockage and liquid water accumulation. By combining these two points, the best case should be a high, uniform temperature in the cathode PTL.

The biggest contribution to the water flux in the membrane came from the mass-charge coupling term (electro-osmosis). Most of the water transport took place due to charge transfer. At a certain current density, the accumulation of water at the cathode became so high, that back-diffusion set in. This balance of phenomena in the membrane is well documented in the literature.[39] The mass-heat coupling term (thermal diffusion) was smaller. We saw that water moved due to thermal osmosis from the cold to the hot side, as described by Kim and Mench,[38] and increased nearly linearly with an increase in current density.

Study 2.—In this section, we report results for varying boundary conditions and compare them to the Base Case. We first increased the temperature on both sides from 340 K to 350 K at 70% relative humidity. In the next step, we applied the temperature differences, as given in Table III.

The results are reported in Tables IV to VI. The first observation is that the cell potential decreased with decreasing temperature, cf. also Fig. 4 and Table V. This is as expected from the thermodynamic relation $F(dE/dT)_p = \Delta S$. Nevertheless, several experiments have shown,[40,41] that a higher temperature in practice leads to a better performance in term of power output. This may be due to operational

Table IV. Temperature jumps at the anode and cathode in K as well as absolute temperatures at the membrane side of the anode and cathode at 1000 and 13500 A m^{-2} for the Base Case and Case 1 to 5 in Study 2.

	1000 A m^{-2}				13500 A m^{-2}			
	$\Delta_{a,m}T$ [K]	$T^{m,a}$ [K]	$\Delta_{m,c}T$ [K]	$T^{m,c}$ [K]	$\Delta_{a,m}T$ [K]	$T^{m,a}$ [K]	$\Delta_{m,c}T$ [K]	$T^{m,c}$ [K]
B	0.25	340.10	0.53	340.09	0.82	346.47	−2.35	348.49
C1	0.32	350.19	0.58	350.18	−0.49	358.74	−4.21	361.55
C2	2.41	342.55	2.70	342.68	3.59	349.88	0.35	352.10
C3	−1.87	342.68	−1.60	342.54	−2.07	349.14	−5.38	351.20
C4	2.34	337.51	2.63	337.65	3.66	343.92	0.61	345.90
C5	−1.85	337.65	−1.58	337.50	−1.99	343.43	−5.08	345.31

Table V. Potential jumps at the anode and cathode as well as cell potential at 1000 and 13500 A m^{-2} for the Base Case and Case 1 to 5 in Study 2 in V.

	1000 A m^{-2}			13500 A m^{-2}		
	$\Delta_{a,m}\phi$ [V]	$\Delta_{m,c}\phi$ [V]	ϕ^{cell} [V]	$\Delta_{a,m}\phi$ [V]	$\Delta_{m,c}\phi$ [V]	ϕ^{cell} [V]
B	−0.287	1.018	0.707	−0.471	0.811	0.254
C1	−0.304	0.994	0.670	−0.516	0.764	0.182
C2	−0.288	1.008	0.701	−0.474	0.786	0.236
C3	−0.294	1.017	0.696	−0.485	0.812	0.239
C4	−0.281	1.019	0.718	−0.460	0.810	0.266
C5	−0.286	1.028	0.714	−0.470	0.829	0.267

conditions, for instance, easier water management. Jang et al.,[42] however, reported, fuel cell stack performance increased only till a certain cell temperature. After this, the hydration of the cell decreased, resulting in a performance drop.

All temperature profiles with 350 K at both boundaries gave the same qualitative behavior, as the Base Case for 340 K (see Table IV). The temperature jumps at the electrodes differed only somewhat in magnitude. Nevertheless, interesting details were seen: At the maximum current density, the PTL temperature at the anode was higher, by up to 3 K, than the PTL side temperature of the cathode. Such behavior has been reported in the literature,[36] however the cell temperature was lower (338 K). Also interesting was the negative water flux at the anode, which had a larger absolute value at 340 than at 350 K (comparing the values −0.04 and −0.08 mol m^{-2} s at 14000 A m^{-2}). Water could obviously leave the cell also by back-diffusion to the anode, if the cathode source term became large enough. Another important observation was that at the maximum current density of 14000 A m^{-2}, the PTL side of the anode was warmer than the membrane side, which was the opposite to the Base Case but in agreement with observations from Viet et al.[36] The reason for this is the significant impact of the Dufour effect, which led to the sign change of the temperature jump. The water flux, which influences the Dufour effect, had a higher negative magnitude, therefore further reducing the temperature jump.

By imposing a temperature difference of 5 K between the boundaries (see Table III for temperature values), we observed dramatic changes in various locations. When the cathode PTL side was cooled, the temperature jumps became bigger on both electrodes for typical values of the current density (see Table IV). We were clearly extracting heat from the cell in the direction of the cathode, and we lowered the temperature peaks. The cooler cathode side introduced an increase in the heat flux out of the cathode and a reduction in the heat flux out of the anode. The results were a more uniform distribution in the cell, smaller entropy production (−0.8% for Case 3 and −1.8% for Case 5). In essence, such knowledge could be used to design and optimize auxiliary cooling systems.

Comparing the results in the IV—and power density curves (Fig. 4), with the help of Table V, we can draw the following conclusions: Having a lower temperature at the cathode side gave a better performance than having a decrease on the anode side. Case 4 and 5 had, generally speaking, already a performance increase compared to Case 1 because the temperatures in the system were usually smaller (as discussed at the beginning of this section). Looking at Case 4, the voltage output of the fuel cell increased approximately 12 mV, whereas in Case 5 it increased around 13 mV. Case 2 and 3 increased the heat in the system, leading to a decrease in cell performance. However, we saw again that a cooler cathode is beneficial (3 mV difference), even more than in Case 4 and 5.

To further see the effect of having different temperatures, according to Table III, at the system boundaries, the contributions to the heat fluxes, namely the Dufour effect, the Peltier effect, and the Fourier heat, in the different parts of the system were analysed in the Base Case and Study 2 to 5.

Table VI gives a summary of the changes in the various contributions in different layers of the fuel cell at 13 500 A m^{-2}. This table provides the change in the measurable heat flux J_q' (see fourth table quadrant) at three locations (Anode PTL, Membrane, Cathode PTL), and the change in the contributions from the Peltier term (first table quadrant), Fourier type term (second table quadrant) and Dufour term (third table quadrant). The changes are reported as % difference of the Base Case value.

When the temperature difference was 5 K between the left and right-hand side, the contribution of the Peltier heat (Table VI first three columns in the upper table) changes between −2.3% and 2.3%. Case 4 and 5 had an overall reduction of the Peltier effect, due to the generally lower temperatures in the homogenous layer. For Case 2 and 3, it was the opposite. This change was quite small since the Peltier coefficient π only depends on the absolute temperature, which was, compared to the magnitude of the temperature gradient change, insignificant. The Fourier and Dufour contributions differed more significantly with values between 12 and −7% for the first and 31 and −65% for the latter one.

The Fourier heat contribution (Table VI last three columns in the upper table) saw more significant changes compared to the Peltier heat effect, due to its dependence on the temperature gradient instead of the absolute temperature. Between Case 2 and 3 and Case 4 and 5

Table VI. Relative change of the overall heat flux J_q' and its contributions in % for the anode PTL, membrane and cathode PTL at 13500 A m^{-2} with respect to the Base Case.

	Peltier a PTL	Peltier m	Peltier c PTL	Fourier a PTL	Fourier m	Fourier c PTL
Δ B/C2 [%]	0.1	1	2.1	9.9	11.7	−1.3
Δ B/C3 [%]	2.3	0.8	−0.1	8.5	1.5	−0.8
Δ B/C4 [%]	−2.3	−0.7	0.1	−7.4	−1.5	0.9
Δ B/C5 [%]	0	−0.9	−2.1	−4.4	−6.9	−1.1
	Dufour a PTL	Dufour m	Dufour c PTL	J_q' a PTL	J_q' m	J_q' c PTL
Δ B/C2 [%]	−8.0	−0.4	8.6	13.2	32.4	−28.2
Δ B/C3 [%]	30.9	8.5	−15.5	−10.5	−19.7	17.5
Δ B/C4 [%]	−64.9	−9.9	11.8	8.8	13.7	−26.3
Δ B/C5 [%]	16.1	3.3	−14.6	−15.3	−44.4	16.7

we observed a difference in sign in the anode PTL and membrane. Case 2 and 3 had higher temperature gradients in those two homogeneous layers, therefore increasing the relative contribution from the Fourier heat effect. For the other two cases, it was the opposite. In the cathode PTL, the temperature gradient was smaller in Case 2 and 4 (where we had a cooler anode) and larger in Case 3 and 5 compared to the Base Case, leading to a reduction and respectively increase in Fourier heat.

The Dufour effect contributions (Table VI first three columns in the lower table) changes in different ways. When the anode side was colder than the cathode side, the contribution decreased in the anode PTL and membrane, whereas for Case 3 and 5 we had the opposite. These observations could be linked to the change in the water flux in these homogenous layers because the heat of transfer coefficient changed only marginal with an increase or decrease of the temperature (5 K temperature difference change q^* for around 1,7%). Having a cooler anode led to a lower water flux directly decreasing the Dufour effect. The same reasoning was also found in the cathode PTL; however, a cooler anode increased the water flux on the cathode side.

As already discussed, imposing a temperature difference at the boundaries of 5 K changed the overall heat flux J_q' significantly (Table VI last three columns in the lower table). Having a cooler anode (Case 2 and 4), increased the heat flux in the anode PTL and membrane and decreased it in the cathode PTL, advanced the asymmetry of it in the fuel cell. A cooler cathode, on the other hand, achieved the adverse effect and led to a more symmetric heat flux. It also lowered the entropy production in the system.

This detailed comparison of the changes in the contributions to the overall heat fluxes in the fuel cell had not been computed before for the best of our knowledge.

Practical implications.—The 1D model presented here, exchanges heat and mass only at the endpoints of the $x-$axis. The other boundaries are adiabatic. This is not so in reality. The temperature profiles, obtained here, could, therefore, be regarded as maximum values when compared to experiments. The model was, nevertheless, an efficient tool for estimation of fluxes in a qualitative and quantitative way, in and out of the cell. Certain FFP patterns exist which can be easily connected to the cell model. These are the bio-inspired tree or fractal-like patterns[43,44] with uniform flow distribution.[45] These patterns can be subdivided into several subcells with one outlet branch. Therefore they can be connected to our 1D model, for a complete fuel cell system analysis. Thereby, we obtain an efficient cell model, which can be solved with a significant reduction in computation time, but which nevertheless captures the essence of the processes, and can be used for predictions, i.e. of local heat and water fluxes, as discussed in Study 1 and 2.

The entropy balance was actively used in the development of the present model to check for model consistency, such as the investigation of the water equilibrium assumption at the electrode surfaces. This is not yet standard procedure but can be recommended especially for validation of thermodynamic properties. A deviation, even a singularity, could immediately be seen in the entropy production error if enthalpy values were wrong.

One of the interesting observations of this model, that may have a practical bearing on PEMFC stack design, is the observation that cathode cooling leads to a higher power density.

Conclusions

We have presented a non-equilibrium thermodynamic 1D-model of a PEM fuel cell, using a state-of-the-art, open-source code[20] as a starting point. The entropy balance was actively used to check for model consistency. The model added detailed information about coupling effects, such as the Soret/Dufour and Seebeck/Peltier effect, and supplemented in this manner to conventional analyses of the fuel cell.

We have shown that the Dufour effects in the homogeneous layers had the same magnitude, but an opposite sign of the Fourier type contribution to the heat flux. Therefore it must not be neglected. The Peltier effects were also substantial. Coupling terms, additionally, had significant contributions to the effective water flux. By imposing a temperature difference of 5 K between inlets/outlets of the cell, we could significantly alter the magnitude of the heat flux, J_q' (up to 44%). Changes in contributions to the overall heat flux J_q' differed between the anode PTL, membrane and the cathode PTL due to different temperature gradients and water fluxes. An important finding in Study 2 was that a cooler cathode is beneficial to the overall performance of the fuel cell for most current densities and in addition, provided a more uniform heat flux distribution in homogenous layers of the fuel cell. This has to be investigated further in experiments. The presented model included the possibility for phase transition of water only at the electrode surfaces. Future work should allow for condensation/evaporation also in the PTLs and create an interface with flow field models.

Acknowledgments

We gratefully acknowledge the support from NTNU in Trondheim and the Research Council of Norway through its Centre of Excellence funding scheme with Project No. 262644 (PoreLab).

ORCID

Marco Sauermoser https://orcid.org/0000-0002-4124-1930
Signe Kjelstrup https://orcid.org/0000-0003-1235-5709
Bruno G. Pollet https://orcid.org/0000-0002-4928-7378

References

1. T. S. Uyar and D. Beşikci, *Int. J. Hydrog. Energy*, **42**, 2453 (2017).
2. J. Wang, H. Wang, and Y. Fan, *Engineering*, **4**, 352 (2018).
3. P. Rodatz, F. Büchi, C. Onder, and L. Guzzella, *J. Power Sources*, **128**, 208 (2004).
4. J. Wu, X. Z. Yuan, J. J. Martin, H. Wang, J. Zhang, J. Shen, S. Wu, and W. Merida, *J. Power Sources*, **184**, 104 (2008).
5. Y. Saygili, I. Eroglu, and S. Kincal, *Int. J. Hydrog. Energy*, **40**, 615 (2015).
6. M. Sauermoser, G. Fossati, N. Kizilova, and S. Kjelstrup, *ECS Trans.*, **92**, 279 (2019).
7. A. F. Gunnarshaug, S. Kjelstrup, D. Bedeaux, F. Richter, and O. S. Burheim, *Electrochim. Acta*, **337**, 135567 (2020).
8. D. M. Bernardi and M. W. Verbrugge, *AIChE J.*, **37**, 1151 (1991).
9. K. Broka and P. Ekdunge, *J. Appl. Electrochem.*, **27**, 281 (1997).
10. A. Z. Weber and J. Newman, *J. Electrochem. Soc.*, **153**, A2205 (2006).
11. S. Kjelstrup and D. Bedeaux, *Non-equilibrium Thermodynamics Of Heterogeneous Systems* (World Scientific, London) Series on Advances in Statistical Mechanics, 2nd ed., 16 (2008).
12. S. Kjelstrup and A. Røsjorde, *J. Phys. Chem. B*, **109**, 9020 (2005).
13. S. Kjelstrup and D. Bedeaux, "Thermodynamics of electrochemical systems." *Springer Handbook of Electrochemical Energy*, ed. C. Breitkopf and K. Swider-Lyons (Springer, Berlin, Heidelberg) Springer Handbooks, 4, p. 69 (2017).
14. M. Siemer, T. Marquardt, G. V. Huerta, and S. Kabelac, *J. Non-Equilib. Thermodyn.*, **42**, 1 (2017).
15. G. V. Huerta, V. Flasbart, T. Marquardt, P. Radici, and S. Kabelac, *Entropy*, **20**, 1 (2018).
16. T. J. Bvumbe, P. Bujlo, I. Tolj, K. Mouton, G. Swart, S. Pasupathi, and B. G. Pollet, *Hydrogen and Fuel Cells*, **1**, 1 (2016).
17. Y. Zong, B. Zhou, and A. Sobiesiak, *J. Power Sources*, **161**, 143 (2006).
18. A. Kulikovsky, *Electrochem. Commun.*, **9**, 6 (2007).
19. J. C. Garcia Navarro, "Modeling a proton exchange membrane fuel cell using non-equilibrium thermodynamics: a second law analysis of assumptions and parameters." *Master's Thesis*, Faculty of Applied Science, TU Delft, Netherlands (2014), http://resolver.tudelft.nl/uuid:b83838fc-847d-4302-800f-434aa64d51fb.
20. R. Vetter and J. O. Schumacher, *Comput. Phys. Commun.*, **234**, 223 (2019).
21. R. O'Hayre, S. Cha, W. Colella, and F. B. Prinz, *Fuel Cell Fundamentals* (John Wiley & Sons, Inc., Hoboken) (2016).
22. H. Meng, *J. Power Sources*, **162**, 426 (2006).
23. A. L. Rangel-Cárdenas and G. J. M. Koper, *Materials*, **10**, 576 (2017).
24. T. E. Springer, T. A. Zawodzinski, and S. Gottesfeld, *J. Electrochem. Soc.*, **138**, 2334 (1991).
25. R. Schweiss, S. Hofmeister, C. Meiser, D. Dan, A. Baumann, T. Kuster, N. Haak, S. Bacher, and G. Korus, "Our gas diffusion layer." *Powering up fuel cells*, SGL CARBON GmbH (2019), https://www.sglcarbon.com/pdf/SIGRACET-Whitepaper.pdf.
26. O. Burheim, P. J. S. Vie, J. G. Pharoah, and S. Kjelstrup, *J. Power Sources*, **195**, 249 (2010).

27. R. B. Bird, W. E. Stewart, and E. N. Lightfoot, *Transport Phenomena* (Wiley, New York) Revised 2nd ed. (2007).
28. W. Grot, "Appendix C—solution cast nafion film." *Fluorinated Ionomers* (William Andrew Publishing, Oxford) PDL Handbook Series, 2nd ed., p. 251 (2011).
29. C. Song, Y. Tang, J. L. Zhang, J. Zhang, H. Wang, J. Shen, S. McDermid, J. Li, and P. Kozak, *Electrochim. Acta*, **52**, 2552 (2007).
30. A. F. Gunnarshaug, S. Kjelstrup, and D. Bedeaux, *Chem. Phys. Lett.: X*, **5**, 100040 (2020).
31. B. E. Poling, J. M. Prausnitz, and J. P. O'onnell, *The Properties of Gases and Liquids* (McGraw-Hill, New York) 5th ed. (2001).
32. A. Z. Weber and J. Newman, *Chem. Rev.*, **104**, 4679 (2004).
33. S. M. Rahgoshay, A. A. Ranjbar, A. Ramiar, and E. Alizadeh, *Energy*, **134**, 61 (2017).
34. W. Yuan, Y. Tang, M. Pan, Z. Li, and B. Tang, *Renew. Energy*, **35**, 656 (2010).
35. A. Rowe and X. Li, *J. Power Sources*, **102**, 82 (2001).
36. P. J. Vie and S. Kjelstrup, *Electrochim. Acta*, **49**, 1069 (2004).
37. R. Zaffou, J. Yi, R. Kunz, and J. Fenton, *ECS Trans.*, **1**, 429 (2006).
38. S. Kim and M. Mench, *J. Membr. Sci.*, **328**, 113 (2009).
39. Q. Yan, H. Toghiani, and J. Wu, *J. Power Sources*, **158**, 316 (2006).
40. Q. Yan, H. Toghiani, and H. Causey, *J. Power Sources*, **161**, 492 (2006).
41. M. Amirinejad, S. Rowshanzamir, and M. H. Eikani, *J. Power Sources*, **161**, 872 (2006).
42. J. H. Jang, H. C. Chiu, W. M. Yan, and W. L. Sun, *J. Power Sources*, **180**, 476 (2008).
43. P. Trogadas, J. I. S. Cho, T. P. Neville, J. Marquis, B. Wu, D. J. L. Brett, and M. O. Coppens, *Energy Environ. Sci.*, **11**, 136 (2018).
44. J. Cho et al., *Energy*, **170**, 14 (2019).
45. M. Sauermoser, S. Kjelstrup, N. Kizilova, B. G. Pollet, and E. G. Flekkøy, *Phys. Chem. Chem. Phys.*, **22**, 6993 (2020).